

Journal of Nanophotonics

Nanophotonics.SPIEDigitalLibrary.org

On optical-absorption peaks in a nonhomogeneous thin-film solar cell with a two-dimensional periodically corrugated metallic backreflector

Faiz Ahmad
Tom H. Anderson
Benjamin J. Civiletti
Peter B. Monk
Akhlesh Lakhtakia

SPIE.

Faiz Ahmad, Tom H. Anderson, Benjamin J. Civiletti, Peter B. Monk, Akhlesh Lakhtakia, "On optical-absorption peaks in a nonhomogeneous thin-film solar cell with a two-dimensional periodically corrugated metallic backreflector," *J. Nanophoton.* **12**(1), 016017 (2018), doi: 10.1117/1.JNP.12.016017.

On optical-absorption peaks in a nonhomogeneous thin-film solar cell with a two-dimensional periodically corrugated metallic backreflector

Faiz Ahmad,^a Tom H. Anderson,^b Benjamin J. Civiletti,^b
Peter B. Monk,^b and Akhlesh Lakhtakia^{a,*}

^aPennsylvania State University, Department of Engineering Science and Mechanics,
NanoMM–Nanoengineered Metamaterials Group, University Park, Pennsylvania, United States

^bUniversity of Delaware, Department of Mathematical Sciences, Newark, Delaware,
United States

Abstract. The rigorous coupled-wave approach (RCWA) was implemented to investigate optical absorption in a triple-*p-i-n*-junction amorphous-silicon solar cell with a two-dimensional (2-D) metallic periodically corrugated backreflector (PCBR). Both total and useful absorptances were computed against the free-space wavelength λ_0 for both *s*- and *p*-polarized polarization states. The useful absorptance in each of the three *p-i-n* junctions was also computed for normal as well as oblique incidence. Furthermore, two canonical boundary-value problems were solved for the prediction of guided-wave modes (GWMs): surface-plasmon-polariton waves and waveguide modes. Use of the doubly periodic PCBR enhanced both useful and total absorptances in comparison with a planar backreflector. The predicted GWMs were correlated with the peaks of the total and useful absorptances. The excitation of GWMs was mostly confined to $\lambda_0 < 700$ nm and enhanced absorption. As excitation of certain GWMs could be correlated with the total absorptance but not with the useful absorptance, the useful absorptance should be studied while devising light-trapping strategies. © 2018 Society of Photo-Optical Instrumentation Engineers (SPIE) [DOI: [10.1117/1.JNP.12.016017](https://doi.org/10.1117/1.JNP.12.016017)]

Keywords: amorphous silicon; guided-wave mode; periodically corrugated backreflector; surface-plasmon-polariton wave; thin-film solar cell; total absorptance; useful absorptance.

Paper 17164SSP received Oct. 20, 2017; accepted for publication Jan. 31, 2018; published online Mar. 6, 2018.

1 Introduction

Amorphous silicon (a-Si) thin-film solar cells provide a viable option to the first-generation crystalline-silicon (c-Si) solar cells,¹ due to their ease of manufacturing and low cost. But the typical efficiency of a-Si thin-film solar cells is not as high as of c-Si solar cells, due to the high electron–hole recombination rate and low charge-carrier diffusion lengths in a-Si.^{2,3} Consequently, light-trapping techniques are necessary to enhance the efficiency of a-Si thin-film solar cells. Several light-trapping strategies have been studied both experimentally and theoretically.^{4,5} Antireflection coatings,^{6–8} textured front faces,^{9,10} metallic periodically corrugated backreflectors (PCBRs),^{11–13} particle plasmonics,¹⁴ surface plasmonics^{15–17} and multiplasmonics,^{18–20} and waveguide-mode excitation^{21–23} are attractive for trapping light in solar cells.

Of particular interest is the enhancement of the optical electric field through the excitation of two types of guided-wave modes (GWMs): surface-plasmon-polariton (SPP) waves and waveguide modes (WGMs). The periodically corrugated interface of a metal and a semiconductor that is periodically nonhomogeneous in the thickness direction (identified by the *z*-axis in Sec. 2) can guide multiple SPP waves at the same frequency.^{18,24} Any open-face waveguide with an air/semiconductor/metal architecture can guide WGMs.^{22,23,25} Therefore, the incorporation of

*Address all correspondence to: Akhlesh Lakhtakia, E-mail: akhlesh@psu.edu

nonhomogeneity along the thickness direction in the semiconductor layers of a solar cell with a PCBR can enhance photonic absorption.^{18,21,26} That enhancement would increase the generation rate of electron–hole pairs.^{26,27}

Much of the theoretical and experimental research done on thin-film solar cells with metallic PCBRs are confined to devices with a homogeneous semiconductor layer and a metallic back-reflector with one-dimensionally (1-D) periodic corrugation. An experimental report of broadband excitation of multiple SPP waves in a device comprising a 1-D photonic crystal (PC) atop a 1-D PCBR²⁸ confirmed theoretical predictions²⁹ and spurred research on solar cells containing piecewise nonhomogeneous semiconductor layers and 1-D PCBRs.^{18,26,27,30} In a recent study, experimental excitation of multiple SPP waves and WGMs were reported in a device comprising a 1-D PC atop a two-dimensional (2-D) PCBR.²¹ Appropriately designed 2-D PCBRs were found to be better for the excitation of GWMs than 1-D PCBRs, after the broadband excitation of GWMs predicted by solving two canonical boundary-value problems was correlated with the experimentally measured absorption spectra.

In solar-cell research, often the excitation of GWMs is correlated with the total absorptance \bar{A}^{tot} of the device,^{18,23} which, however, is not a good measure of useful photonic absorption in a solar cell, as photons absorbed in the metallic portions of a solar cell are not available for conversion into electric current. Therefore, the chief objective for the work reported in this paper was to determine the spectra of both the total absorptance \bar{A}^{tot} and the useful absorptance \bar{A}^{sc} ³¹ in a tandem solar cell with a 2-D PCBR exposed to either normally or obliquely incident linearly polarized light. The solar cell was taken to comprise three *p-i-n* solar cells made of a-Si alloys³² that can be fabricated using plasma-enhanced chemical-vapor deposition over planar and patterned substrates. A top layer of aluminum-doped zinc oxide (AZO) was incorporated to provide a transparent electrode. Also, an AZO layer was taken to be sandwiched between the 2-D PCBR and the stack of nine semiconductor layers to avoid the deterioration of the electrical properties of the a-Si alloy closest to the metal,³³ which was chosen to be silver.³⁴ The total absorptance and the useful absorptance calculated using the rigorous coupled-wave approach (RCWA)^{24,35,36} were correlated against the predicted excitations of GWMs.

The plan of this paper is as follows: Sec. 2 is divided into four parts. Section 2.1 presents the boundary-value problem that can be solved to determine the optical electromagnetic fields everywhere in a device comprising a stratified, isotropic dielectric material atop a 2-D PCBR when the device is illuminated by a plane wave. The formulations for useful and total absorptances are discussed in Sec. 2.2. Section 2.3 provides brief descriptions of the underlying canonical problems to predict the excitation of SPP waves and WGMs. Excitation of GWMs is discussed in Sec. 2.4. Section 3 is divided into two parts. The wavenumbers of the predicted GWMs are presented in Sec. 3.1. Correlations of the absorptances with the predicted GWMs are discussed in Sec. 3.2. The paper concludes with some remarks in Sec. 4.

An $\exp(-i\omega t)$ dependence on time t is implicit, with ω denoting the angular frequency and $i = \sqrt{-1}$. The free-space wavenumber, the free-space wavelength, and the intrinsic impedance of free space are denoted by $k_0 = \omega\sqrt{\mu_0\epsilon_0}$, $\lambda_0 = 2\pi/k_0$, and $\eta_0 = \sqrt{\mu_0/\epsilon_0}$, respectively, with μ_0 being the permeability and ϵ_0 the permittivity of free space. Vectors are underlined; the Cartesian unit vectors are identified as \hat{u}_x , \hat{u}_y , and \hat{u}_z ; and column vectors as well as matrices are in boldface.

2 Theory in Brief

2.1 Boundary-Value Problem for Tandem Solar Cell

Let us consider the boundary-value problem shown in Fig. 1 for a tandem solar cell containing three *p-i-n* junctions. The solar cell occupies the region $\mathcal{X}: \{(x, y, z) | -\infty < x < \infty, -\infty < y < \infty, 0 < z < L_t\}$, with the half spaces $z < 0$ and $z > L_t$ occupied by air. The reference unit cell is identified as $\mathcal{R}: \{(x, y, z) | -L_x/2 < x < L_x/2, -L_y/2 < y < L_y/2, 0 < z < L_t\}$, the backreflector being periodic along both the x - and y -axes.

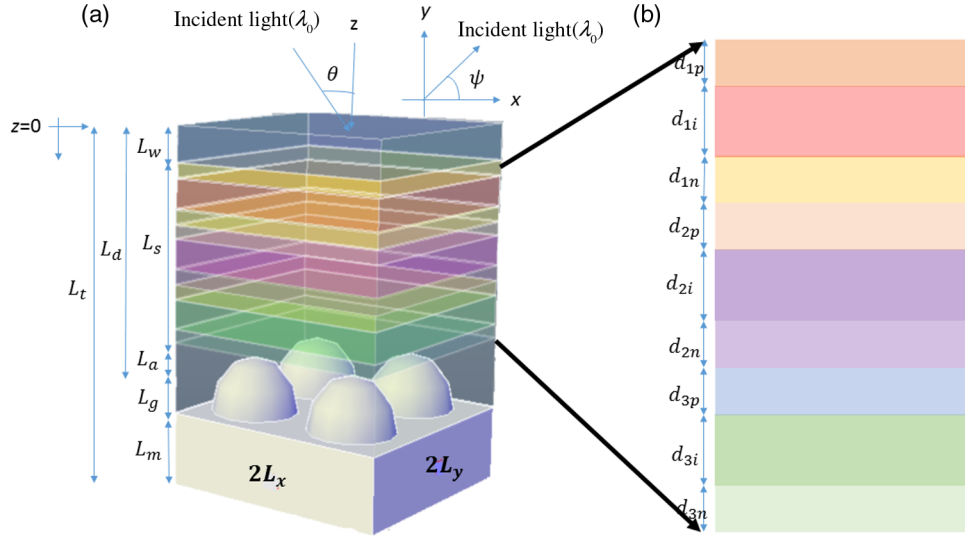


Fig. 1 (a) Schematic of the tandem solar cell comprising three *p-i-n* junctions of a-Si alloys on a 2-D PCBR. The wavevector of the incident plane wave is inclined at angle θ with respect to the z -axis and angle ψ with respect to the x -axis in the xy plane. (b) Nine semiconductor layers of the three *p-i-n* junctions.

The region $0 < z < L_d = L_w + L_s + L_a$ is occupied by a cascade of homogeneous layers and is compactly characterized by the permittivity $\varepsilon_d(z, \lambda_0)$, which is a piecewise constant function of z . The top layer $0 < z < L_w$ and the bottom layer $L_w + L_s < z < L_d$ are made of AZO with permittivity $\varepsilon_w(\lambda_0)$. The semiconductor layers in the region $L_w < z < L_w + L_s$ are identified in Fig. 1(b). The region $L_d + L_g < z < L_d + L_g + L_m$ is occupied by a metal with permittivity $\varepsilon_m(\lambda_0)$.

The region $L_d < z < L_d + L_g$, henceforth termed the grating region, contains a periodically undulating surface with period L_x along the x -axis and period L_y along the y -axis, respectively. In the grating region, \mathcal{X} possesses rectangular symmetry in the xy plane. The permittivity $\varepsilon_g(x, y, z, \lambda_0)$ in the grating region can be stated as

$$\varepsilon_g(x, y, z, \lambda_0) = \varepsilon_m(\lambda_0) + [\varepsilon_w(\lambda_0) - \varepsilon_m(\lambda_0)]\mathcal{U}[z - g_1(x)]\mathcal{U}[z - g_2(y)],$$

$$|x| < \zeta_x L_x / 2, \quad |y| < \zeta_y L_y / 2, \quad z \in (L_d, L_d + L_g), \quad (1)$$

where the unit step function

$$\mathcal{U}(\sigma) = \begin{cases} 0, & \sigma < 0, \\ 1, & \sigma \geq 0, \end{cases} \quad (2)$$

and $\zeta_x \in [0, 1]$ as well as $\zeta_y \in [0, 1]$ are the duty cycles. We chose the grating-shape functions

$$g_1(x) = \begin{cases} L_d + L_g \left[1 - \cos\left(2\pi \frac{\pi x}{\zeta_x L_x}\right) \right], & x \in \left(-\frac{\zeta_x L_x}{2}, \frac{\zeta_x L_x}{2}\right) \\ L_d + L_g, & x \notin \left(-\frac{\zeta_x L_x}{2}, \frac{\zeta_x L_x}{2}\right) \end{cases} \quad (3)$$

and

$$g_2(y) = \begin{cases} L_d + L_g \left[1 - \cos\left(2\pi \frac{\pi y}{\zeta_y L_y}\right) \right], & y \in \left(-\frac{\zeta_y L_y}{2}, \frac{\zeta_y L_y}{2}\right) \\ L_d + L_g, & y \notin \left(-\frac{\zeta_y L_y}{2}, \frac{\zeta_y L_y}{2}\right) \end{cases} \quad (4)$$

to represent hillocks for all data reported in this paper. The grating-shape functions chosen here are only for illustration, many other choices fit for experimental study being also available.¹³

Suppose that an arbitrarily polarized plane wave, propagating in the half space $z < 0$ at an angle $\theta \in [0 \text{ deg}, 90 \text{ deg})$ with respect to the z -axis and an angle $\psi \in [0 \text{ deg}, 360 \text{ deg})$ with respect to the x -axis in the xy plane, is incident on the plane $z = 0$. The electric field phasor of this plane wave can be stated as

$$\underline{E}_{\text{inc}}(\underline{r}) = [\bar{a}_s \underline{s}^{(0,0)} + \bar{a}_p \underline{p}_+^{(0,0)}] \exp\{i[\underline{\kappa}^{(0,0)} + \alpha_0^{(0,0)} \hat{u}_z] \cdot \underline{r}\}, \quad (5)$$

where \bar{a}_s and \bar{a}_p are the known coefficients of s - and p -polarized components, respectively. Here and hereafter, the following quantities are used:

$$\left. \begin{aligned} \underline{\kappa}^{(m,n)} &= k_x^{(m)} \hat{u}_x + k_y^{(n)} \hat{u}_y \\ k_x^{(m)} &= k_0 \sin \theta \cos \psi + m(2\pi/L_x) \\ k_y^{(n)} &= k_0 \sin \theta \sin \psi + n(2\pi/L_y) \\ k_{xy}^{(m,n)} &= +\sqrt{\underline{\kappa}^{(m,n)} \cdot \underline{\kappa}^{(m,n)}} \\ \alpha_0^{(m,n)} &= +\sqrt{k_0^2 - \underline{\kappa}^{(m,n)} \cdot \underline{\kappa}^{(m,n)}} \\ \underline{s}^{(m,n)} &= -\frac{k_y^{(n)}}{k_{xy}^{(m,n)}} \hat{u}_x + \frac{k_x^{(m)}}{k_{xy}^{(m,n)}} \hat{u}_y \\ \underline{p}_+^{(m,n)} &= -\left[\frac{k_x^{(m)}}{k_{xy}^{(m,n)}} \hat{u}_x + \frac{k_y^{(n)}}{k_{xy}^{(m,n)}} \hat{u}_y \right] \frac{\alpha_0^{(m,n)}}{k_0} + \frac{k_{xy}^{(m,n)}}{k_0} \hat{u}_z \\ \underline{p}_-^{(m,n)} &= \left[\frac{k_x^{(m)}}{k_{xy}^{(m,n)}} \hat{u}_x + \frac{k_y^{(n)}}{k_{xy}^{(m,n)}} \hat{u}_y \right] \frac{\alpha_0^{(m,n)}}{k_0} + \frac{k_{xy}^{(m,n)}}{k_0} \hat{u}_z \end{aligned} \right\}, \quad m \in \mathbb{Z}, \quad n \in \mathbb{Z}. \quad (6)$$

As a result of the metallic PCBR being doubly periodic, the x - and y -dependences of the electric and magnetic field phasors are represented everywhere as an infinite series of Floquet harmonics as^{24,35,36}

$$\left. \begin{aligned} \underline{E}(x, y, z) &= \sum_{m \in \mathbb{Z}} \sum_{n \in \mathbb{Z}} \underline{e}^{(m,n)}(z) \exp[i \underline{\kappa}^{(m,n)} \cdot \underline{r}] \\ \underline{H}(x, y, z) &= \sum_{m \in \mathbb{Z}} \sum_{n \in \mathbb{Z}} \underline{h}^{(m,n)}(z) \exp[i \underline{\kappa}^{(m,n)} \cdot \underline{r}] \end{aligned} \right\}, \quad (7)$$

where

$$\left. \begin{aligned} \underline{e}^{(m,n)}(z) &= e_x^{(m,n)}(z) \hat{u}_x + e_y^{(m,n)}(z) \hat{u}_y + e_z^{(m,n)}(z) \hat{u}_z \\ \underline{h}^{(m,n)}(z) &= h_x^{(m,n)}(z) \hat{u}_x + h_y^{(m,n)}(z) \hat{u}_y + h_z^{(m,n)}(z) \hat{u}_z \end{aligned} \right\} \quad (8)$$

are expansion coefficients. Accordingly, the incident and the reflected electric field phasors are represented as

$$\left. \begin{aligned} \underline{E}_{\text{inc}}(x, y, z) &= \sum_{m \in \mathbb{Z}} \sum_{n \in \mathbb{Z}} ([a_s^{(m,n)} \underline{s}^{(m,n)} + a_p^{(m,n)} \underline{p}_+^{(m,n)}] \exp\{i[\underline{\kappa}^{(m,n)} + \alpha_0^{(m,n)} \hat{u}_z] \cdot \underline{r}\}) \\ \underline{E}_{\text{ref}}(x, y, z) &= \sum_{m \in \mathbb{Z}} \sum_{n \in \mathbb{Z}} ([r_s^{(m,n)} \underline{s}^{(m,n)} + r_p^{(m,n)} \underline{p}_-^{(m,n)}] \exp\{i[\underline{\kappa}^{(m,n)} - \alpha_0^{(m,n)} \hat{u}_z] \cdot \underline{r}\}) \end{aligned} \right\}, \quad z < 0, \quad (9)$$

and the transmitted electric field phasor as

$$\underline{E}_{\text{tr}}(x, y, z) = \sum_{m \in \mathbb{Z}} \sum_{n \in \mathbb{Z}} ([t_s^{(m,n)} \underline{s}^{(m,n)} + t_p^{(m,n)} \underline{p}_+^{(m,n)}] \exp\{i[\underline{\kappa}^{(m,n)} + \alpha_0^{(m,n)} \hat{u}_z] \cdot (\underline{r} - L_t \hat{u}_z)\}), \quad z > L_t, \quad (10)$$

where the coefficients $a_s^{(m,n)} = \bar{a}_s \delta_{m0} \delta_{n0}$ and $a_p^{(m,n)} = \bar{a}_p \delta_{m0} \delta_{n0}$ in Eqs. (9) are known with $\delta_{mm'}$ denoting the Kronecker delta, but the coefficients $r_s^{(m,n)}$, $r_p^{(m,n)}$, $t_s^{(m,n)}$, and $t_p^{(m,n)}$ in Eqs. (9) and (10) have to be determined. Finally, the permittivity $\varepsilon(x, y, z)$ everywhere is represented by the Fourier series

$$\varepsilon(x, y, z) = \sum_{m \in \mathbb{Z}} \sum_{n \in \mathbb{Z}} \varepsilon^{(m,n)}(z) \exp\{i[\underline{\kappa}^{(m,n)} - \underline{\kappa}^{(0,0)}] \cdot \underline{r}\}, \quad (11)$$

where $\varepsilon^{(m,n)}(z)$ are Fourier coefficients.

Computational tractability requires the expansions in Eqs. (7)–(11) to be truncated to include only $m \in \{-M_t, \dots, M_t\}$ and $n \in \{-N_t, \dots, N_t\}$, with $M_t \geq 0$ and $N_t \geq 0$. Furthermore, a superindex

$$\tau = m(2N_t + 1) + n, \quad m \in [-M_t, M_t], \quad n \in [-N_t, N_t], \quad (12)$$

is defined for convenience. Then, $\tau \in [-\tau_t, \tau_t]$, where $\tau_t = 2M_tN_t + M_t + N_t$. Also, both the mapping from (m, n) to τ and the inverse mapping from τ to (m, n) are injective.³⁷ Thereafter, column vectors

$$\begin{aligned} \check{\mathbf{e}}_\sigma(z) &= [e_\sigma^{(-\tau_t)}(z), e_\sigma^{(-\tau_t+1)}(z), \dots, e_\sigma^{(\tau_t-1)}(z), e_\sigma^{(\tau_t)}(z)]^T \\ \check{\mathbf{h}}_\sigma(z) &= [h_\sigma^{(-\tau_t)}(z), h_\sigma^{(-\tau_t+1)}(z), \dots, h_\sigma^{(\tau_t-1)}(z), h_\sigma^{(\tau_t)}(z)]^T \end{aligned} \quad \sigma \in \{x, y, z\}, \quad (13)$$

of length $2\tau_t + 1$ are set up, the superscript T denoting the transpose. The Toeplitz matrix³⁸

$$\check{\mathbf{e}}(z) = \begin{bmatrix} \check{e}^{(-\tau_t, -\tau_t)}(z) & \check{e}^{(-\tau_t, -\tau_t+1)}(z) & \dots & \check{e}^{(-\tau_t, \tau_t-1)}(z) & \check{e}^{(-\tau_t, \tau_t)}(z) \\ \check{e}^{(-\tau_t+1, -\tau_t)}(z) & \check{e}^{(-\tau_t+1, -\tau_t+1)}(z) & \dots & \check{e}^{(-\tau_t+1, \tau_t-1)}(z) & \check{e}^{(-\tau_t+1, \tau_t)}(z) \\ \dots & \dots & \dots & \dots & \dots \\ \check{e}^{(\tau_t-1, -\tau_t)}(z) & \check{e}^{(\tau_t-1, -\tau_t+1)}(z) & \dots & \check{e}^{(\tau_t-1, \tau_t-1)}(z) & \check{e}^{(\tau_t-1, \tau_t)}(z) \\ \check{e}^{(\tau_t, -\tau_t)}(z) & \check{e}^{(\tau_t, -\tau_t+1)}(z) & \dots & \check{e}^{(\tau_t, \tau_t-1)}(z) & \check{e}^{(\tau_t, \tau_t)}(z) \end{bmatrix} \quad (14)$$

contains the Fourier coefficients appearing in Eq. (8) with $\check{e}^{(\tau, \tau')}(z) = e^{(m-m', n-n')}(z)$. Finally, the $(2\tau_t + 1) \times (2\tau_t + 1)$ Fourier-wavenumber matrices

$$\begin{aligned} \check{\mathbf{K}}_x &= \text{diag}[\check{k}_x^{(-\tau_t)}, \check{k}_x^{(-\tau_t+1)}, \dots, \check{k}_x^{(\tau_t-1)}, \check{k}_x^{(\tau_t)}] \\ \check{\mathbf{K}}_y &= \text{diag}[\check{k}_y^{(-\tau_t)}, \check{k}_y^{(-\tau_t+1)}, \dots, \check{k}_y^{(\tau_t-1)}, \check{k}_y^{(\tau_t)}] \end{aligned} \quad (15)$$

are set up with $\check{k}_x^{(\tau)} = k_x^{(m)}$ and $\check{k}_y^{(\tau)} = k_y^{(n)}$.

The frequency-domain Maxwell curl postulates yield the matrix ordinary differential equation²⁴

$$\frac{d}{dz} \check{\mathbf{f}}(z) = i\check{\mathbf{P}}(z) \cdot \check{\mathbf{f}}(z), \quad (16)$$

where the $4(2\tau_t + 1)$ -column vector

$$\check{\mathbf{f}}(z) = \begin{bmatrix} \check{\mathbf{e}}_x(z) \\ \check{\mathbf{e}}_y(z) \\ \check{\mathbf{h}}_x(z) \\ \check{\mathbf{h}}_y(z) \end{bmatrix}, \quad (17)$$

and the $4(2\tau_t + 1) \times 4(2\tau_t + 1)$ matrix

$$\begin{aligned} \check{\mathbf{P}}(z) &= \omega \begin{bmatrix} \check{\mathbf{0}} & \check{\mathbf{0}} & \check{\mathbf{0}} & \mu_0 \check{\mathbf{I}} \\ \check{\mathbf{0}} & \check{\mathbf{0}} & -\mu_0 \check{\mathbf{I}} & \check{\mathbf{0}} \\ \check{\mathbf{0}} & -\check{\mathbf{e}}(z) & \check{\mathbf{0}} & \check{\mathbf{0}} \\ \check{\mathbf{e}}(z) & \check{\mathbf{0}} & \check{\mathbf{0}} & \check{\mathbf{0}} \end{bmatrix} \\ &+ \frac{1}{\omega} \begin{bmatrix} \check{\mathbf{0}} & \check{\mathbf{0}} & \check{\mathbf{K}}_x \cdot [\check{\mathbf{e}}(z)]^{-1} \cdot \check{\mathbf{K}}_y & -\check{\mathbf{K}}_x \cdot [\check{\mathbf{e}}(z)]^{-1} \cdot \check{\mathbf{K}}_x \\ \check{\mathbf{0}} & \check{\mathbf{0}} & \check{\mathbf{K}}_y \cdot [\check{\mathbf{e}}(z)]^{-1} \cdot \check{\mathbf{K}}_y & -\check{\mathbf{K}}_y \cdot [\check{\mathbf{e}}(z)]^{-1} \cdot \check{\mathbf{K}}_x \\ -\mu_0^{-1} \check{\mathbf{K}}_x \cdot \check{\mathbf{K}}_y & \mu_0^{-1} \check{\mathbf{K}}_x \cdot \check{\mathbf{K}}_x & \check{\mathbf{0}} & \check{\mathbf{0}} \\ -\mu_0^{-1} \check{\mathbf{K}}_y \cdot \check{\mathbf{K}}_y & \mu_0^{-1} \check{\mathbf{K}}_y \cdot \check{\mathbf{K}}_x & \check{\mathbf{0}} & \check{\mathbf{0}} \end{bmatrix}, \end{aligned} \quad (18)$$

contains $\mathbf{\check{0}}$ as the $(2\tau_t + 1) \times (2\tau_t + 1)$ null matrix and $\mathbf{\check{I}}$ as the $(2\tau_t + 1) \times (2\tau_t + 1)$ identity matrix.

To solve Eq. (16), the region \mathcal{R} is partitioned into a sufficiently large number of thin slices along the z -direction.²⁴ Each slice is taken to be homogeneous along the z -axis, but it is either homogeneous or periodically nonhomogeneous along the x - and y -axes; thus, $\mathbf{\check{P}}(z)$ is assumed to be uniform in each slice. Boundary conditions are enforced on the planes $z = 0$ and $z = L_t$ to match the fields to the incident, reflected, and transmitted waves, as appropriate. A stable numerical marching algorithm is then used to determine the Fourier coefficients of the electric and magnetic field phasors in each slice.²⁴ Finally, the z components of the electric and magnetic field phasors in the device can be obtained through $\check{\mathbf{e}}_z(z) = -[\omega\epsilon(z)]^{-1} \cdot [\check{\mathbf{K}}_x \cdot \check{\mathbf{h}}_y(z) - \check{\mathbf{K}}_y \cdot \check{\mathbf{h}}_x(z)]$ and $\check{\mathbf{h}}_z(z) = (\omega\mu_0)^{-1} [\check{\mathbf{K}}_x \cdot \check{\mathbf{e}}_y(z) - \check{\mathbf{K}}_y \cdot \check{\mathbf{e}}_x(z)]$. Thus, the electric field phasor can be determined everywhere. The entire procedure was implemented on the Mathematica[®] platform.

2.2 Total and Useful Absorptances

At any location inside the device, the absorption rate of the monochromatic optical energy per unit volume is given by

$$Q(x, y, z) = \frac{1}{2} \omega \operatorname{Im}\{\epsilon(x, y, z)\} |E(x, y, z)|^2. \quad (19)$$

The useful absorptance³⁹

$$\bar{A}^{\text{sc}} = \frac{2\eta_0}{L_x L_y (|\bar{a}_s|^2 + |\bar{a}_p|^2) \cos \theta} \iiint_{\mathcal{R}_{\text{sc}}} Q(x, y, z) dx dy dz \quad (20)$$

is calculated by integrating $Q(x, y, z)$ over the region $\mathcal{R}_{\text{sc}} \subset \mathcal{R}$ occupied by the semiconductor layers. Likewise, absorptance in the metal is given by

$$\bar{A}^{\text{met}} = \frac{2\eta_0}{L_x L_y (|\bar{a}_s|^2 + |\bar{a}_p|^2) \cos \theta} \iiint_{\mathcal{R}_{\text{met}}} Q(x, y, z) dx dy dz, \quad (21)$$

where $\mathcal{R}_{\text{met}} \subset \mathcal{R}$ is the region occupied by the metal. The total absorptance is then the sum

$$\bar{A}^{\text{tot}} = \bar{A}^{\text{sc}} + \bar{A}^{\text{met}}, \quad (22)$$

if ϵ_w is purely real.

Four reflection and four transmission coefficients of order (m, n) are defined as the elements in the 2×2 matrices appearing in the following relations:²⁴

$$\begin{bmatrix} r_s^{(m,n)} \\ r_p^{(m,n)} \end{bmatrix} = \begin{bmatrix} r_{ss}^{(m,n)} & r_{sp}^{(m,n)} \\ r_{ps}^{(m,n)} & r_{pp}^{(m,n)} \end{bmatrix} \cdot \begin{bmatrix} \bar{a}_s \\ \bar{a}_p \end{bmatrix}, \quad \begin{bmatrix} t_s^{(m,n)} \\ t_p^{(m,n)} \end{bmatrix} = \begin{bmatrix} t_{ss}^{(m,n)} & t_{sp}^{(m,n)} \\ t_{ps}^{(m,n)} & t_{pp}^{(m,n)} \end{bmatrix} \cdot \begin{bmatrix} \bar{a}_s \\ \bar{a}_p \end{bmatrix}. \quad (23)$$

Coefficients of order $(0,0)$ are classified as specular, whereas coefficients of all other orders are nonspecular. Four reflectances and four linear transmittances of order (m, n) are defined as

$$R_{\text{sp}}^{(m,n)} = \frac{\operatorname{Re}[\alpha_0^{(m,n)}]}{\alpha_0^{(0,0)}} |r_{\text{sp}}^{(m,n)}|^2 \in [0,1], \quad (24)$$

etc., and two absorptances as

$$\left. \begin{aligned} A_s &= 1 - \sum_{m=-M_t}^{m=M_t} \sum_{n=-N_t}^{n=N_t} [R_{\text{ss}}^{(m,n)} + R_{\text{ps}}^{(m,n)} + T_{\text{ss}}^{(m,n)} + T_{\text{ps}}^{(m,n)}] \in [0,1] \\ A_p &= 1 - \sum_{m=-M_t}^{m=M_t} \sum_{n=-N_t}^{n=N_t} [R_{\text{pp}}^{(m,n)} + R_{\text{sp}}^{(m,n)} + T_{\text{pp}}^{(m,n)} + T_{\text{sp}}^{(m,n)}] \in [0,1] \end{aligned} \right\}. \quad (25)$$

These are total absorptances in that they contain the contributions of the semiconductors and the metal in the solar cell. Whereas \bar{A}^{tot} , \bar{A}^{sc} , and \bar{A}^{met} are defined for incident light of arbitrary polarization state, A_s is defined for incident s -polarized light, and A_p for incident p -polarized light. All absorptances presented in Sec. 3 were calculated for a solar cell comprising just one triple p - i - n junction, as shown in Fig. 1.

2.3 Canonical Boundary-Value Problems

Two separate canonical boundary-value problems were solved to correlate peaks in the spectra of various absorptances with the excitation of SPP waves and WGMs. Details on both canonical problems are available elsewhere³⁹ for the interested reader, but we note the following salient features of both canonical problems.

2.3.1 SPP waves

The complex-valued wavenumbers $q \neq 0$ of SPP waves for a specific value of λ_0 were obtained by solving a canonical boundary-value problem,^{24,29} with the assumptions that the backreflector metal occupies the half space $z < 0$, a periodically semi-infinite cascade of three p - i - n junctions that occupy the half space $z > 0$, and there are no AZO layers.

2.3.2 Waveguide modes

An open-faced waveguide is formed by the three p - i - n junctions interposed between two half spaces, one occupied by air and the other by the backreflector metal of thickness considerably exceeding the skin depth.⁴⁰ For a specific value of λ_0 , this waveguide can support the propagation of multiple WGMs (with wavenumbers $q \neq 0$), which can play significant light-trapping roles.²¹⁻²³ We ignored the AZO layers for this canonical problem as well.

2.4 Excitation of SPP Waves and WGMs

Planewave illumination will excite a GWM of wavenumber q as a Floquet harmonic of order (m, n) , provided that²⁴

$$\pm \text{Re}[q] \simeq k_{xy}^{(m,n)}. \quad (26)$$

When $L_x = L_y = L$, the right side of Eq. (26) simplifies to yield

$$\pm \text{Re}[q/k_0] \simeq \{[\sin \theta + (m \cos \psi + n \sin \psi)(\lambda_0/L)]^2 + [(m \sin \psi - n \cos \psi)(\lambda_0/L)]^2\}^{\frac{1}{2}}. \quad (27)$$

Since the thickness L_d is finite, shifts in the predictions of θ for specific values of λ_0 and ψ are possible for SPP waves. Also, shifts are possible for both SPP waves and WGMs because both canonical problems were formulated and solved with $L_w = L_a = 0$. Finally, shifts can also be due to $L_g \neq 0$.⁴¹ Therefore, for all absorptance spectra presented in this paper, we accepted predictions of θ from Eq. (27) with ± 1 deg tolerance. However, let us note that not every possible GWM is strongly excited by planewave illumination.

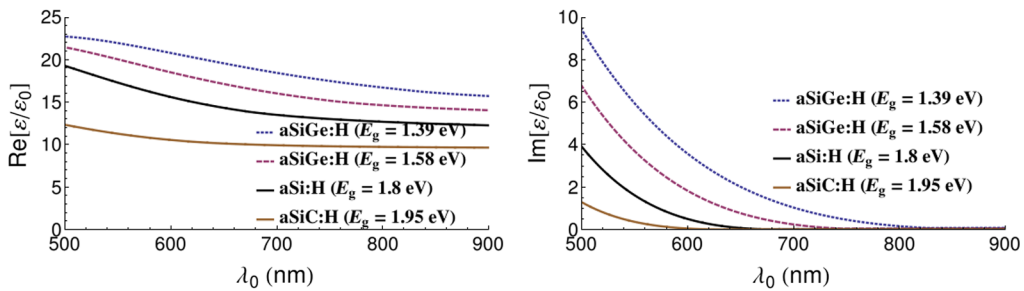
Finally, it is important to note that depolarization can occur because the PCBR is doubly periodic. Accordingly, illumination by a linearly polarized plane wave for a specific value of ψ can excite a GWM of a different polarization state propagating in a direction specified by the angle φ that may differ from ψ .^{21,42}

3 Numerical Results and Discussion

All optical and geometric parameters were chosen only to illustrate the relationships of the WGMs to total and useful absorptances but still are representative of actual tandem solar

Table 1 Compositions, band gaps, and thicknesses of hydrogenated a-Si alloys used for the nine semiconductor layers in the triple-*p-i-n*-junction tandem solar cell.

Layer	Composition	Bandgap (eV)	Thickness (nm)
1 <i>p</i>	a-Si _{1-<i>u</i>} C _{<i>u</i>} :H	1.95	20
1 <i>i</i>	a-Si:H	1.8	200
1 <i>n</i>	a-Si:H	1.8	20
2 <i>p</i>	a-Si _{1-<i>u</i>} C _{<i>u</i>} :H	1.95	20
2 <i>i</i>	a-Si _{1-<i>u</i>} Ge _{<i>u</i>} :H	1.58	200
2 <i>n</i>	a-Si:H	1.8	20
3 <i>p</i>	a-Si:H	1.8	20
3 <i>i</i>	a-Si _{1-<i>u</i>} Ge _{<i>u</i>} :H	1.39	200
3 <i>n</i>	a-Si:H	1.8	20


Fig. 2 Spectra of the relative permittivity $\varepsilon/\varepsilon_0$ of the different semiconductor alloys used in the triple-*p-i-n*-junction tandem solar cell.

cells.³⁰ The compositions, band gaps, and thicknesses of the nine hydrogenated a-Si alloys for the nine semiconductor layers are presented in Table 1. The permittivity of each alloy was calculated as a function of λ_0 , using a model provided by Ferlauto et al.^{18,32} The spectra of all nine permittivities, normalized by ε_0 , are plotted in Fig. 2. The 2-D PCBR was taken to be made of silver.³⁴ The refractive index of AZO was taken as a function of λ_0 from Gao et al.⁴³

The following dimensions were chosen: $L_w = 100$ nm, $L_a = 60$ nm, $L_g = 80$ nm, $L_m = 30$ nm, $L_x = L_y = 400$ nm, and $\zeta_x = \zeta_y = 1$. We used $M_t = N_t$ accordingly. Furthermore, we used $M_t \leq 12$, which ensured the convergence of all nonzero reflectances and absorptances to within $\pm 1\%$ for every $\lambda_0 \in \{500, 502, \dots, 898, 900\}$ nm. Here, convergence was defined to have occurred when there was a difference not exceeding 1% in magnitude between the results for $M_t = N - 1$ and $M_t = N$. Higher values of M_t were found to be necessary for higher λ_0 as the chosen semiconductor alloys are then less absorbing and the effect of grating is more pronounced.

3.1 Prediction of GWM Wavenumbers

The real parts of the normalized wavenumbers q/k_0 of SPP waves are presented in Fig. 3 as functions of $\lambda_0 \in \{500, 501, \dots, 899, 900\}$ nm. These wavenumbers are organized into three branches (labeled *s1* – *s3*) for *s*-polarized SPP waves and seven branches (labeled *p1* – *p7*) for *p*-polarized SPP waves. The real parts of the normalized wavenumbers q/k_0 of the WGMs are presented in Fig. 4. These wavenumbers are arranged into six branches for both *s*- and *p*-polarized WGMs labeled *s1* – *s6* and *p1* – *p6*, respectively.

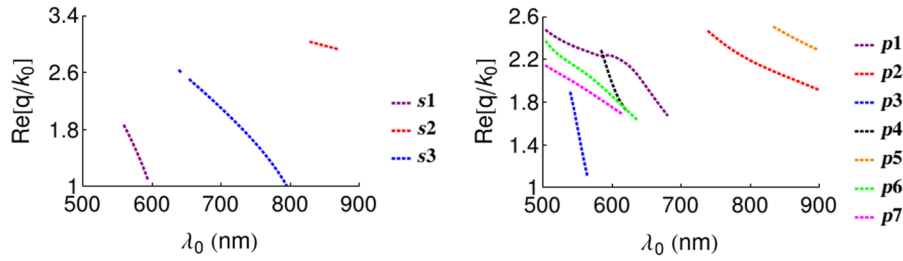


Fig. 3 Real parts of the normalized wavenumbers q/k_0 of s - and p -polarized SPP waves obtained after solving the relevant canonical boundary-value problem.

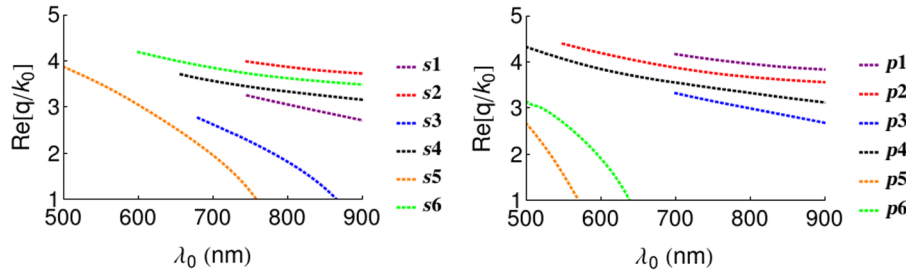


Fig. 4 Real parts of the normalized wavenumbers q/k_0 of s - and p -polarized WGMs obtained after solving the relevant canonical boundary-value problem.

3.2 Absorptances and Correlation with Predictions

Calculations of A_s and A_p as functions of $\lambda_0 \in [500, 900]$ nm were made for the chosen triple- p - i - n junction tandem solar cell with a 2-D PCBR. In addition, we computed the spectra of the useful absorptances

$$\left. \begin{aligned} \bar{A}_s^{\text{sc}} &= \bar{A}^{\text{sc}}|_{\bar{a}_p=0} \\ \bar{A}_p^{\text{sc}} &= \bar{A}^{\text{sc}}|_{\bar{a}_s=0} \end{aligned} \right\} \quad (28)$$

The spectra of A_s , A_p , \bar{A}_s^{sc} , and \bar{A}_p^{sc} for $\lambda_0 \in [500, 900]$ nm for solar cells with and without corrugations ($L_g = 80$ nm and $L_g = 0$, respectively) were examined for several combinations of θ and ψ .³⁹ For the sake of illustration, data are presented in Figs. 5–8 only for the following two directions of incidence:

1. $\{\psi = 1 \text{ deg}, \theta = 1 \text{ deg}\}$, and
2. $\{\psi = 45 \text{ deg}, \theta = 15 \text{ deg}\}$.

The choice of 1 deg instead of 0 deg for the incidence angles helps avoid spurious results associated with the computation of distinct eigenvalues of $\check{\mathbf{P}}(z)$ when the RCWA is implemented. Also shown in these figures are the spectra of the useful absorptances \bar{A}_s^{scm} and \bar{A}_p^{scm} in the m 'th p - i - n junction, $m \in \{1, 2, 3\}$, for incident s - and p -polarized plane waves, respectively.

The excitation of a GWM is marked by an absorptance peak. Therefore, values of $\lambda_0 \in [500, 900]$ nm for which the solutions of the two canonical problems (with the assumption that $L_w = L_a = 0$) predicted the excitation of SPP waves and WGMs for $\theta \in [0 \text{ deg}, 2 \text{ deg}] \cup [14 \text{ deg}, 16 \text{ deg}]$ are also identified in Figs. 5–8. Red arrows indicate the excitation of SPP waves that matched with both total absorptances (A_s and A_p) and useful absorptances (\bar{A}_s^{sc} and \bar{A}_p^{sc}); black arrows indicate WGMs that matched with both total absorptances and useful absorptances; blue arrows indicate the excitation of SPP waves that correlated with total absorptances but not with useful absorptances; and purple arrows indicate the excitation of WGMs that correlated with total absorptances but not with useful absorptances.

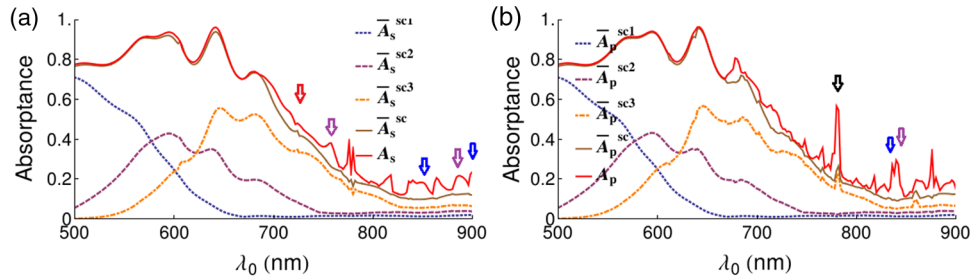


Fig. 5 Spectra of (a) A_s , \bar{A}_s^{sc} , \bar{A}_s^{sc1} , \bar{A}_s^{sc2} , and \bar{A}_s^{sc3} and (b) A_p , \bar{A}_p^{sc} , \bar{A}_p^{sc1} , \bar{A}_p^{sc2} , and \bar{A}_p^{sc3} of the triple-*p-i-n*-junction tandem solar cell, when $\psi = 1$ deg and $\theta = 1$ deg. Red arrows indicate the excitation of SPP waves that matched with both total absorptances (A_s and A_p) and useful absorptances (\bar{A}_s^{sc} and \bar{A}_p^{sc}); black arrows indicate WGMs that matched with both total absorptances and useful absorptances; blue arrows indicate the excitation of SPP waves that correlated with total absorptances but not with useful absorptances; and purple arrows indicate the excitation of WGMs that correlated with total absorptances but not with useful absorptances.

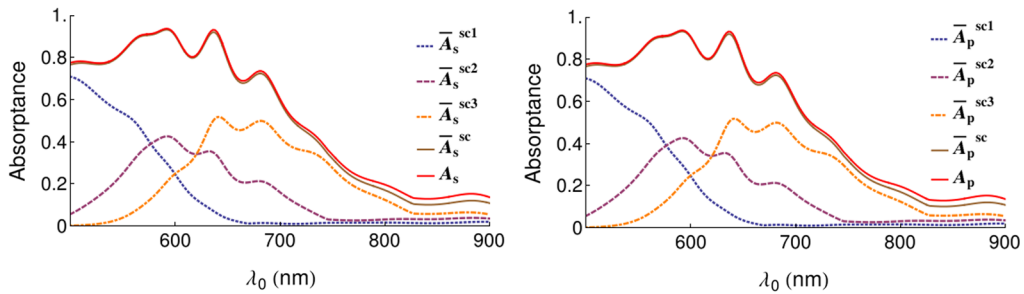


Fig. 6 Same as Fig. 5 except that $L_g = 0$.

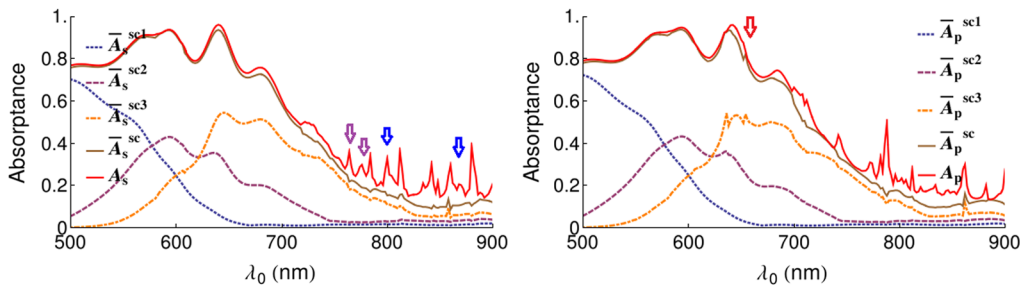


Fig. 7 Same as Fig. 5, except that $\theta = 15$ deg and $\psi = 45$ deg.

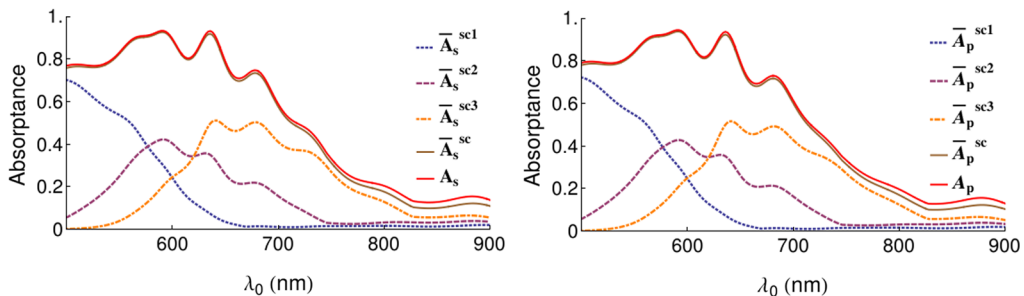


Fig. 8 Same as Fig. 7, except that $L_g = 0$.

Table 2 Values of $\lambda_0 \in [500,900]$ nm (calculated at 1-nm intervals) for which the excitation of an SPP wave as a Floquet harmonic of order (m, n) is predicted for $\theta \in [0 \text{ deg}, 2 \text{ deg}]$ and $\psi = 1 \text{ deg}$, for the tandem solar cell with a 2-D PCBR. The SPP waves strongly excited in Fig. 5 are highlighted in bold.

Pol. state	λ_0 (nm)	$\text{Re}\{q/k_0\}$	θ deg	(m, n)
s	730	1.816	0.856	(1,0)
s	845	2.988	0.088	(1,1)
<i>p</i>	570	2.027	0.991	(1,1)
<i>p</i>	640	2.029	1.024	($\pm 1,0$)
<i>p</i>	680	1.678	1.228	(1,0)
p	897	2.988	0.847	(1,0)

3.2.1 Case 1: $\{\psi = 1 \text{ deg}, \theta = 1 \text{ deg}\}$

Spectra of A_s , A_p , \bar{A}_s^{sc} , and \bar{A}_p^{sc} for $\{\psi = 1 \text{ deg}, \theta = 1 \text{ deg}\}$ calculated with $L_g = 80 \text{ nm}$ are presented in Fig. 5. Also, spectra of the same quantities calculated with $L_g = 0$ are presented in Fig. 6 for comparison. Tables 2 and 3 contain values of $\lambda_0 \in [500,900]$ nm for which the excitation of either an SPP wave or a WGM as a Floquet harmonic of order (m, n) is predicted.

The \bar{A}_s^{sc} -peak at $\lambda_0 \approx 728 \text{ nm}$ in Fig. 5 occurs close to the wavelength $\lambda_0 \approx 730 \text{ nm}$ predicted for the excitation of an *s*-polarized SPP wave as a Floquet harmonic of order (1,0) at $\theta = 0.856 \text{ deg}$ as shown in Table 2. This is the only SPP wave that correlated with peaks of both \bar{A}_s^{sc} and A_s .

The A_s -peak in Fig. 5 at

- $\lambda_0 \approx 845 \text{ nm}$ is due to the excitation of an *s*-polarized SPP wave as a Floquet harmonic of order (1,1) predicted at $\theta = 0.088 \text{ deg}$ in Table 2.
- $\lambda_0 \approx 897 \text{ nm}$ matches well with the excitation of a *p*-polarized SPP wave as a Floquet harmonic of order (1,0) predicted at $\theta = 0.847 \text{ deg}$ in Table 2.
- $\lambda_0 \approx 754 \text{ nm}$ is related with the excitation of a *p*-polarized WGM as a Floquet harmonic of order (-2,0) predicted at $\theta = 1.145 \text{ deg}$ in Table 3.
- $\lambda_0 \approx 892 \text{ nm}$ is the excitation of a *p*-polarized WGM as a Floquet harmonic of order (-1,1) predicted at $\theta = 1.198 \text{ deg}$ in Table 3.

Excitation of these GWMs correlated only with the total absorptance A_s but not with the useful absorptance \bar{A}_s^{sc} , which indicates that not every \bar{A}_s^{sc} -peak can be matched to an

Table 3 Same as Table 2, except that the relevant excitations of WGMs are indicated. The WGMs strongly excited in Fig. 5 are highlighted in bold.

Pol. state	λ_0 (nm)	$\text{Re}\{q/k_0\}$	θ deg	(m, n)
<i>s</i>	663	3.685	1.334	(-2,1)
<i>s</i>	711	3.536	1.076	(-2,0)
s	786	1.948	0.948	(-1,0)
s	834	2.938	0.838	(-1,1)
<i>s</i>	898	3.163	0.902	(-1,1)
p	754	3.750	1.145	(-2,0)
<i>p</i>	797	3.963	1.206	(-2,0)
<i>p</i>	827	2.910	1.121	(-1,1)
p	892	3.138	1.198	(-1,1)

A_s -peak that is correlated with the excitation of a GWM.^{21,44} Accordingly, useful absorptance, not the overall absorptance, needs to be studied for solar cells. Contributions to the overall absorptance are made both by the semiconductor layers and the metallic PCBR, but the contribution of the latter is useless for harvesting solar energy.

The \bar{A}_p^{sc} -peak in Fig. 5 at $\lambda_0 \approx 786$ nm is due to the excitation of an s -polarized WGM as a Floquet harmonic of order $(-1,0)$ predicted at $\theta = 0.948$ deg in Table 3. The A_p -peak at

- $\lambda_0 \approx 834$ nm is due to the excitation of a p -polarized WGM as a Floquet harmonic of order $(-1,1)$ predicted at $\theta = 0.838$ deg in Table 3.
- $\lambda_0 \approx 845$ nm matches well with the excitation of a p -polarized SPP wave as a Floquet harmonic of order $(1,1)$ predicted at $\theta = 0.088$ deg in Table 2.

On comparing Figs. 5 and 6, we note that the GWMs are excited at $\lambda_0 > 700$ nm. Also, the total absorptance for $L_g = 80$ nm exceeds that for $L_g = 0$ in the same spectral regime. This increase is largely due to the increases in $\bar{A}_s^{\text{sc}3}$ and $\bar{A}_p^{\text{sc}3}$, i.e., in the p - i - n junction closest to the PCBR. Furthermore, increases in both total and useful absorptances for $\lambda_0 \in [634,680]$ nm, regardless of the polarization state of the incident light, were observed with the use of the PCBR rather than a planar backreflector. In addition, depolarization due to the 2-D periodicity of the PCBR is evident from the excitation of WGMs that are not of the same polarization state as the incident light.

3.2.2 Case 2: $\{\psi = 45 \text{ deg}, \theta = 15 \text{ deg}\}$

Calculated spectra of A_s , A_p , \bar{A}_s^{sc} , and \bar{A}_p^{sc} for $\{\psi = 45 \text{ deg}, \theta = 15 \text{ deg}\}$ with $L_g = 80$ nm are presented in Fig. 7. Also, the spectra A_s , A_p , \bar{A}_s^{sc} , and \bar{A}_p^{sc} calculated with $L_g = 0$ for the same incident direction are presented in Fig. 8. Tables 4 and 5 contain values of $\lambda_0 \in [500,900]$ nm for which the excitation of either an SPP wave or a WGM as a Floquet harmonic of order (m, n) is predicted from analysis of Figs. 3 and 4.

No \bar{A}_s^{sc} -peak could be correlated with the excitation of a GWM. The A_s -peak at

- $\lambda_0 \approx 800$ nm is related to the excitation of a p -polarized SPP wave as a Floquet harmonic of order either $(1,0)$ or $(0,1)$ predicted at $\theta = 14.952$ deg in Table 4.
- $\lambda_0 \approx 870$ nm is due to the excitation of a p -polarized SPP wave as a Floquet harmonic of order either $(-1,0)$ or $(0,-1)$ predicted at $\theta = 15.880$ deg in Table 4.
- $\lambda_0 \approx 764$ nm is associated with the excitation of a p -polarized WGM as a Floquet harmonic of order $(-1,-2)$ predicted at $\theta = 15.141$ deg in Table 5.
- $\lambda_0 \approx 778$ nm arises due to the excitation of a p -polarized WGM as a Floquet harmonic of order either $(-2,0)$ or $(0,-2)$ predicted at $\theta = 15.411$ deg in Table 5.

Table 4 Values of $\lambda_0 \in [500,900]$ nm (calculated at 1-nm intervals) for which the excitation of an SPP wave as a Floquet harmonic of order (m, n) is predicted for $\theta \in [0 \text{ deg}, 2 \text{ deg}]$ and $\psi = 45 \text{ deg}$, for the tandem solar cell backed by a 2-D PCBR. The SPP waves strongly excited in Fig. 7 are highlighted in bold.

Pol. state	λ_0 (nm)	$\text{Re}\{q/k_0\}$	θ deg	(m, n)
s	647	2.581	15.529	(1,1)
s	690	2.193	14.231	$(-1, -1)$
p	565	2.272	15.955	$(1, 1)$
p	620	1.734	14.365	$(1, 0), (0, 1)$
p	750	2.404	14.315	$(-1, -1)$
p	800	2.190	14.952	(1,0), (0,1)
p	870	2.376	15.880	$(-1, 0), (0, -1)$

Table 5 Same as Table 4, except that the relevant excitations of WGMs are indicated. The WGMs strongly excited in Fig. 7 are highlighted in bold.

Pol. state	λ_0 (nm)	$\text{Re}\{q/k_0\}$	θ deg	(m, n)
s	732	3.484	15.004	(-2,0), (0,-2)
s	807	3.858	14.931	(-2,0), (0,-2)
p	764	4.023	15.141	(-1, -2)
p	778	3.706	15.411	(-2, 0), (0, -2)
p	664	3.641	14.287	(-2,1)
p	732	3.477	15.355	(-2,0), (0,-2)
p	821	3.925	15.098	(-2,0), (0,-2)

The \bar{A}_p^{sc} -peak at $\lambda_0 \approx 647$ nm is related with the excitation of an *s*-polarized SPP wave as a Floquet harmonic of order (1,1) at $\theta = 15.529$ deg in Table 4. No other \bar{A}_p^{sc} - or A_p -peak was found to be correlated with GWM excitation. These results underscore the fact that useful absorptance is not necessarily enhanced by the excitation of a GWM. However, there are useful- and total-absorptance peaks that could not predicted by the canonical boundary-value problems.

On comparing Figs. 7 and 8, increases in both total and useful absorptances for $\lambda_0 \in [640,670]$ nm, regardless of the polarization state of the incident light, become evident with the use of the PCBR rather than a planar backreflector. On comparison with normal illumination (Sec. 3.2.1) for which GWMs were excited only for $\lambda_0 > 700$ nm, an SPP wave is excited at $\lambda_0 = 647$ nm for oblique illumination. This is in accord with the blueshifts of SPP waves expected for oblique illumination^{18,42} as well as with the angular trends in Figs. 3 and 4.

Apart from the SPP wave excited at $\lambda_0 = 647$ nm, all other GWMs are excited at $\lambda_0 > 700$ nm. The polarization state of an excited GWM may not be the same as that of the incident light because the 2-D PCBR is a depolarizing agent. Finally, the total absorptance increases in the same spectral regime with the use of the PCBR in comparison with a planar backreflector, for either polarization state of the incident light, which is largely due to the increases in $\bar{A}_s^{\text{sc}3}$ and $\bar{A}_p^{\text{sc}3}$, i.e., in the *p-i-n* junction closest to the PCBR.

4 Concluding Remarks

The effect of a 2-D PCBR on the absorptance of light in a triple-*p-i-n*-junction thin-film solar cell was studied using the RCWA. Total absorptances and useful absorptances for incident *s*- and *p*-polarized light were computed against the free-space wavelength for two different incidence directions. Calculations were also made of the useful absorptance in each of the three *p-i-n* junctions. Furthermore, two canonical boundary-value problems were solved for the prediction of GWMs. The predicted GWMs were correlated with the peaks of the total and useful absorptances for both linear polarization states.

Numerical studies led to the following conclusions:

- Regardless of the illumination direction and the polarization state of the incident light, increases in useful and total absorptances for $\lambda_0 < 700$ nm arise from the replacement of a planar backreflector by a 2-D PCBR.
- The triple-*p-i-n*-junction tandem solar cell made of a-Si alloys is highly absorbing for $\lambda_0 < 700$ nm, so that the excitation of SPP waves in this regime is unnoticeable.
- Both SPP waves and WGMs are excited for $\lambda_0 > 700$ nm for both normal and oblique illumination. An SPP wave excited at $\lambda_0 = 647$ nm for oblique illumination is in accord with blueshifting of SPP waves with increasing obliqueness of illumination.
- Some of the excited GWMs directly contribute to the increase in useful absorptance of the solar cell backed by a 2-D PCBR. This increase is largely due to enhanced absorptance in the *p-i-n* junction closest to the 2-D PCBR.

- Depolarization due to the 2-D periodicity of the PCBR is evident from the excitation of GWMs that are not of the same polarization state as the incident light.
- Excitation of certain GWMs could be correlated with the total absorptance but not with the useful absorptance.

When devising light-trapping strategies, the useful, but not the total absorptance, needs to be focused on. Although reduction of reflectance is a worthwhile objective, meeting it will not necessarily boost the useful absorptance. We conclude with the recommendation that material and geometric parameters need to be optimized for efficiency enhancement.

Acknowledgments

This paper was substantially based on a paper titled, "On optical-absorption peaks in a nonhomogeneous dielectric material over a two-dimensional metallic surface-relief grating," presented at the SPIE Optics and Photonics conference, Nanostructured Thin Films X, held August 5–11, 2017, in San Diego, California, United States. F. Ahmad thanks the Graduate School and the College of Engineering, Pennsylvania State University, for a University Graduate Fellowship during the first year of his doctoral studies. A. Lakhtakia thanks the Charles Godfrey Binder Endowment at the Pennsylvania State University for ongoing support of his research. The research of F. Ahmed and A. Lakhtakia is partially supported by US National Science Foundation (NSF) under Grant No. DMS-1619901. The research of T.H. Anderson, B.J. Civiletti, and P.B. Monk is partially supported by the US National Science Foundation (NSF) under Grant No. DMS-1619904.

References

1. R. Singh, "Why silicon is and will remain the dominant photovoltaic material," *J. Nanophotonics* **3**(1), 032503 (2009).
2. D. E. Carlson and C. R. Wronski, "Amorphous silicon solar cell," *Appl. Phys. Lett.* **28**(11), 671–673 (1976).
3. M. A. Green, "Thin-film solar cells: review of materials, technologies and commercial status," *J. Mater. Sci.* **18**(Suppl. 1), 15–19 (2007).
4. R. Singh, G. F. Alapatt, and A. Lakhtakia, "Making solar cells a reality in every home: opportunities and challenges for photovoltaic device design," *IEEE J. Electron. Dev. Soc.* **1**(6), 129–144 (2013).
5. R. J. Martín-Palma and A. Lakhtakia, "Progress on bioinspired, biomimetic, and bioreplication routes to harvest solar energy," *Appl. Phys. Rev.* **4**(2), 021103 (2017).
6. I. G. Kavakli and K. Kantarli, "Single and double-layer antireflection coatings on silicon," *Turk. J. Phys.* **26**(5), 349–354 (2002).
7. S. K. Dhungel et al., "Double-layer antireflection coating of $\text{MgF}_2/\text{SiN}_x$ for crystalline silicon solar cells," *J. Korean Phys. Soc.* **49**(3), 885–889 (2006).
8. S. A. Boden and D. M. Bagnall, "Sunrise to sunset optimization of thin film antireflective coatings for encapsulated, planar silicon solar cells," *Prog. Photovoltaics Res. Appl.* **17**(4), 241–252 (2009).
9. W. H. Southwell, "Pyramid-array surface-relief structures producing antireflection index matching on optical surfaces," *J. Opt. Soc. Am. A* **8**(3), 549–553 (1991).
10. K. C. Sahoo et al., "Silicon nitride nanopillars and nanocones formed by nickel nanoclusters and inductively coupled plasma etching for solar cell application," *Jpn. J. Appl. Phys.* **48**(12), 126508 (2009).
11. P. Sheng, A. N. Bloch, and R. S. Stepleman, "Wavelength-selective absorption enhancement in thin-film solar cells," *Appl. Phys. Lett.* **43**(6), 579–581 (1983).
12. C. Heine and R. H. Morf, "Submicrometer gratings for solar energy applications," *Appl. Opt.* **34**(14), 2476–2482 (1995).
13. M. Solano et al., "Optimization of the absorption efficiency of an amorphous-silicon thin-film tandem solar cell backed by a metallic surface-relief grating," *Appl. Opt.* **52**(5), 966–979 (2013); erratum: **54**(3), 398–399 (2015).

14. Y. Zhang et al., "Influence of rear located silver nanoparticle induced light losses on the light trapping of silicon wafer-based solar cells," *J. Appl. Phys.* **116**(12), 124303 (2014).
15. L. M. Anderson, "Parallel-processing with surface plasmons, A new strategy for converting the broad solar spectrum," in *Proc. 16th IEEE Photovoltaic Specialist Conf.*, Vol. 1, pp. 371–377 (1982).
16. L. M. Anderson, "Harnessing surface plasmons for solar energy conversion," *Proc. SPIE* **408**(1), 172–178 (1983).
17. M. G. Deceglie et al., "Design of nanostructured solar cells using coupled optical and electrical modeling," *Nano Lett.* **12**(6), 2894–2900 (2012).
18. M. Faryad and A. Lakhtakia, "Enhancement of light absorption efficiency of amorphous-silicon thin-film tandem solar cell due to multiple surface-plasmon-polariton waves in the near-infrared spectral regime," *Opt. Eng.* **52**(8), 087106 (2013); errata: **53**(12), 129801 (2014).
19. M. E. Solano et al., "Buffer layer between a planar optical concentrator and a solar cell," *AIP Adv.* **5**(9), 097150 (2015).
20. L. Liu et al., "Planar light concentration in micro-Si solar cells enabled by a metallic grating–photonic crystal architecture," *ACS Photonics* **3**(4), 604–610 (2016).
21. L. Liu et al., "Experimental excitation of multiple surface-plasmon-polariton waves and waveguide modes in a one-dimensional photonic crystal atop a two-dimensional metal grating," *J. Nanophotonics* **9**(1), 093593 (2015).
22. F.-J. Haug et al., "Excitation of guided-mode resonances in thin film silicon solar cells," in *MRS Symp. Proc.*, Vol. 1321, pp. 123–128 (2011).
23. T. Khaleque and R. Magnusson, "Light management through guided-mode resonances in thin-film silicon solar cells," *J. Nanophotonics* **8**(1), 083995 (2014).
24. J. A. Polo, Jr., T. G. Mackay, and A. Lakhtakia, *Electromagnetic Surface Waves: A Modern Perspective*, Elsevier, Waltham, Massachusetts (2013).
25. A. W. Snyder and J. D. Love, *Optical Waveguide Theory*, Chapman and Hall, New York (1983).
26. T. H. Anderson et al., "Combined optical-electrical finite-element simulations of thin-film solar cells with homogeneous and nonhomogeneous intrinsic layers," *J. Photonics Energy* **6**(2), 025502 (2016).
27. T. H. Anderson, T. G. Mackay, and A. Lakhtakia, "Enhanced efficiency of Schottky-barrier solar cell with periodically nonhomogeneous indium nitride layer," *J. Photonics Energy* **7**(1), 014502 (2017).
28. A. S. Hall et al., "Broadband light absorption with multiple surface plasmon polariton waves excited at the interface of a metallic grating and photonic crystal," *ACS Nano* **7**(6), 4995–5007 (2013).
29. M. Faryad et al., "Excitation of multiple surface-plasmon-polariton waves guided by a periodically corrugated interface of a metal and a periodic multilayered isotropic dielectric material," *J. Opt. Soc. Am. B* **29**(4), 704–713 (2012).
30. M. Faryad et al., "Optical and electrical modeling of an amorphous-silicon tandem solar cell with nonhomogeneous intrinsic layers and a periodically corrugated back-reflector," *Proc. SPIE* **8823**(1), 882306 (2013).
31. M. V. Shuba et al., "Adequacy of the rigorous coupled-wave approach for thin-film silicon solar cells with periodically corrugated metallic backreflectors: spectral analysis," *J. Opt. Soc. Am. A* **32**(7), 1222–1230 (2015).
32. A. S. Ferlauto et al., "Analytical model for the optical functions of amorphous semiconductors from the near-infrared to ultraviolet: applications in thin film photovoltaics," *J. Appl. Phys.* **92**(5), 2424–2436 (2002).
33. S. J. Fonash, *Solar Cell Device Physics*, Academic Press, Burlington, Massachusetts (2010).
34. <http://refractiveindex.info/?group=METALS/material=Silver> (9 July 2017).
35. E. N. Glytsis and T. K. Gaylord, "Rigorous three-dimensional coupled-wave diffraction analysis of single and cascaded anisotropic gratings," *J. Opt. Soc. Am. A* **4**(11), 2061–2080 (1987).
36. M. Onishi, K. Crabtree, and R. A. Chipman, "Formulation of rigorous coupled-wave theory for gratings in bianisotropic media," *J. Opt. Soc. Am. A* **28**(8), 1747–1758 (2011).

37. E. Kreyszig, *Advanced Engineering Mathematics*, 10th ed., Wiley, Hoboken, New Jersey (2011).
38. H. Lütkepohl, *Handbook of Matrices*, Wiley, Chichester, United Kingdom (1996).
39. F. Ahmad et al., "On optical-absorption peaks in a nonhomogeneous dielectric material over a two-dimensional metallic surface-relief grating," *Proc. SPIE* **10356**(1), 103560I (2017).
40. M. F. Iskander, *Electromagnetic Fields and Waves*, 2nd ed., Waveland Press, Long Grove, Illinois (2013).
41. M. V. Shuba and A. Lakhtakia, "Splitting of absorptance peaks in absorbing multilayer backed by a periodically corrugated metallic reflector," *J. Opt. Soc. Am. A* **33**(4), 779–784 (2016).
42. J. Dutta, S. A. Ramakrishna, and A. Lakhtakia, "Characteristics of surface plasmon-polariton waves excited on 2D periodically patterned columnar thin films of silver," *J. Opt. Soc. Am. A* **33**(9), 1697–1704 (2016).
43. X.-Y. Gao, L. Liang, and Q.-G. Lin, "Analysis of the optical constants of aluminum-doped zinc-oxide films by using the single-oscillator model," *J. Korean Phys. Soc.* **57**(4), 710–714 (2010).
44. M. Faryad and A. Lakhtakia, "Grating-coupled excitation of multiple surface plasmon-polariton waves," *Phys. Rev. A* **84**(3), 033852 (2011).

Faiz Ahmad received his MSc and MPhil degrees in electronics from Quaid-i-Azam University, Islamabad (Pakistan) in 2010 and 2012. Currently, he is a PhD student in the Department of Engineering Science and Mechanics at the Pennsylvania State University. His research interests include electromagnetic surface waves and light trapping in thin-film solar cells.

Tom H. Anderson received his MSc degree from the University of York in 2012 for work on modeling of nonlocal transport in Tokamak plasmas. He received his PhD from the University of Edinburgh, UK, in 2016 for his thesis titled "Optoelectronic Simulations of Nonhomogeneous Solar Cells." Currently, he is a postdoctoral researcher at the University of Delaware. His current research interests include optical and electrical modeling of solar cells, numerics, plasma physics, and plasmonics.

Benjamin J. Civiletti received his MA degree in mathematics from Villanova University in 2014. Currently, he is a PhD student in the Department of Mathematical Sciences at the University of Delaware. His research interests include numerical methods for modeling solar cells.

Peter B. Monk is a Unidel professor in the Department of Mathematical Sciences at the University of Delaware. He is the author of *Finite Element Methods for Maxwell's Equations* and coauthor with F. Cakoni and D. Colton of *The Linear Sampling Method in Inverse Electromagnetic Scattering*.

Akhlesh Lakhtakia is the Charles Godfrey Binder professor of engineering science and mechanics at the Pennsylvania State University. His current research interests include surface multiplasmonics, solar cells, sculptured thin films, mimics, bioreplication, and forensic science. He has been elected as a fellow of Optical Society of America, SPIE, Institute of Physics, American Association for the Advancement of Science, American Physical Society, Institute of Electrical and Electronics Engineers, Royal Society of Chemistry, and Royal Society of Arts. He received the 2010 SPIE Technical Achievement Award and the 2016 Walston Chubb Award for Innovation.